



**Michigan  
Technological  
University**

Michigan Technological University  
**Digital Commons @ Michigan Tech**

---

Dissertations, Master's Theses and Master's Reports

---

2022

# OPTICAL AND SINGLE PARTICLE PROPERTIES OF NORTH ATLANTIC FREE TROPOSPHERIC AEROSOLS AND IMPLICATIONS FOR AEROSOL DIRECT RADIATIVE FORCING

Megan Morgenstern  
*Michigan Technological University*, [memorgen@mtu.edu](mailto:memorgen@mtu.edu)

Copyright 2022 Megan Morgenstern

---

## Recommended Citation

Morgenstern, Megan, "OPTICAL AND SINGLE PARTICLE PROPERTIES OF NORTH ATLANTIC FREE TROPOSPHERIC AEROSOLS AND IMPLICATIONS FOR AEROSOL DIRECT RADIATIVE FORCING", Open Access Master's Thesis, Michigan Technological University, 2022.  
<https://doi.org/10.37099/mtu.dc.etr/1377>

Follow this and additional works at: <https://digitalcommons.mtu.edu/etr>



Part of the [Other Physics Commons](#)

OPTICAL AND SINGLE PARTICLE PROPERTIES OF NORTH ATLANTIC FREE  
TROPOSPHERIC AEROSOLS AND IMPLICATIONS FOR AEROSOL DIRECT  
RADIATIVE FORCING

By

Megan E. Morgenstern

A THESIS

Submitted in partial fulfillment of the requirements for the degree of

MASTER OF SCIENCE

In Applied Physics

MICHIGAN TECHNOLOGICAL UNIVERSITY

2022

© 2022 Megan E. Morgenstern

This thesis has been approved in partial fulfillment of the requirements for the Degree of MASTER OF SCIENCE in Applied Physics.

Department of Physics

Thesis Advisor: *Claudio Mazzoleni*

Committee Member: *Raymond Shaw*

Committee Member: *Xin Xi*

Department Chair: *Ravindra Pandey*

# Table of Contents

List of Figures .....	iv
List of Tables .....	v
Acknowledgments.....	vi
Abstract.....	vii
1 Introduction.....	1
2 Methods.....	3
2.1 Observatório da Montanha do Pico (OMP).....	3
2.2 Optical and Radiative Properties.....	3
2.3 Aerosol Sampling and Single Particle Analysis.....	6
2.3.1 Computer-controlled Scanning Electron Microscopy with Energy Dispersive X-ray Spectrometry .....	6
2.3.2 Particle Mixing State Index .....	7
2.4 Particle Concentration and Meteorological Parameters .....	9
2.5 FLEXible PARTicle Dispersion Model .....	9
3 Results and Discussion .....	10
3.1 Optical and Radiative Properties.....	10
3.2 Single Particle Analysis.....	12
3.2.1 CCSEM-EDX .....	12
3.2.2 Mixing State Index.....	15
3.3 Particle Count and Meteorological Parameters .....	15
3.4 FLEXPART.....	16
3.5 Comparison of Samples S5 and S6 .....	18
4 Conclusion .....	24
5 References.....	25
A Appendix.....	29
A.1 Elemental Classification of Samples.....	29
A.2 Correction of C, N, and O .....	29
A.3 Nephelometer LED Spectral Power Distribution Curves.....	29
A.4 Aerosol Forcing Parameter Values.....	30

## List of Figures

Figure 1: A plot of the mixing state index, $\chi$ . Lines of constant $\chi$ are shown in.....	8
Figure 2: The classified chemical composition of the seven samples. The first figure .....	14
Figure 3: FLEXPART retroplumes for seven samples collected in June and July of .....	17
Figure 4: FLEXPART CO tracer simulations for (a) June and (b) July of 2015.....	18
Figure 5: The solar irradiance for samples S5 (left) and S6 (right). The boxes .....	18
Figure 6: The particle counts for channels 1 and 2, as well as the ratio of the channels...	20
Figure 7: Measured scattering and backscattering coefficients for samples S5 (top).....	21
Figure 8: The 5-minute averaged scattering Ångström exponents for samples S5 .....	22
Figure 9: The relative spectral power distribution curves for the Aurora 3000.....	30

## List of Tables

Table 1: Optical properties for the seven samples. The scattering coefficients.....	10
Table 2: A summary of the seven samples including collection date and time,.....	12
Table 3: Average particle species diversity, bulk population species diversity, .....	15
Table 4: Average particle count and meteorological data, plus their respective .....	16
Table 5: Aerosol spectral radiative forcing for samples S5 and S7 above clear sky .....	22

## **Acknowledgments**

I would like to thank my advisor and family for their constant support, encouragement, and mentorship. I would also like to thank Zoe for her help in keeping things in perspective. Without you all, this wouldn't have been possible.

## Abstract

Human-induced climate change has steadily become a reality rather than a possibility. One factor that plays into climate change is radiative forcing due to aerosol-radiation interactions (ARI). As such, it is important to understand how aerosols (atmospheric particles) interact with solar radiation. This work looks at seven samples of well-aged aerosols (aerosols traveling in the atmosphere for at least a few days) collected at Pico Mountain Observatory in the summer of 2015. Pico Mountain Observatory is located in a remote, high elevation site in the Azores, in the Eastern-North Atlantic Ocean. The goals of the study were to analyze the physicochemical properties of these atmospheric particles and to unravel potential relations with their radiative properties.

From single particle analysis, it was found that all samples contained predominantly carbon-based aerosols, with smaller amounts of sea salt and mineral dust observed in some samples. Modeled atmospheric transport paths indicated most sampled particles came from North America with long transport times. The particles in all samples were internally mixed, further supporting the expectation and modeling findings that the sampled particles were well-aged.

Two selected samples, one dominated by biomass burning, and a second affected by mineral dust, were compared in more detail. Radiative forcing calculations have been performed for the particles collected during two events. The calculations were performed for two scenarios with different reflectances of the surfaces underneath: clear sky ocean and clouds. It was found that there is potential cooling over areas of low albedo, such as the clear sky ocean, and potential warming over areas of high albedo, such as above clouds.

# 1 Introduction

Aerosols play an important role in our planet's climate system through their interaction with radiation, especially scattering and absorption of sunlight ([Mitchell, 1971](#)). How efficiently aerosols scatter or absorb radiation, depends on characteristics like the shape, size, morphology, and composition; properties that, in turn, depend also on the age of the aerosol ([Seinfeld & Pandis, 2016](#); [Yao et al., 2022](#)). Understanding the effects of aerosols in the atmosphere is crucial to understanding whether the climate is warming or cooling due to their presence, both globally and regionally. The growing realization that climate change is occurring and that policies and procedures must be implemented to reduce the negative effects of this change means that we must understand what policies and procedures to implement ([Bellouin et al., 2020](#); [Masson-Delmotte et al., 2021](#)). Since it is impossible to make accurate, continuous measurements worldwide of aerosols, modeling is often used to understand the past and present effects ([Myhre et al., 2013](#)), as well as the expected effects decades into the future. Reliance on modeling, however, means that the models must provide an accurate picture of reality, both in the past and present.

Well-aged aerosols in particular have poorly constrained effects on climate due to their unconstrained radiative forcing ([Zheng et al., 2020](#)). Here, 'well-aged' means aerosols that remain suspended in the atmosphere on a timescale of days, though lifetimes of a couple of weeks are possible. Due to the transitory nature of the planetary boundary layer (PBL), the 1-2 kilometers of atmosphere closest to the Earth, aerosols in this layer do not tend to be well-aged. Instead, an extended residence occurs in the free troposphere, the atmospheric layer above the PBL up to the tropopause, which allows for aerosols to travel hundreds of kilometers from their emission sources ([Cheng et al., 2022](#)). As they travel, aerosols undergo physical and chemical changes, often further complicating already complex aerosol properties and their interactions ([Dunlea et al., 2009](#); [Rudich et al., 2007](#); [Zheng et al., 2020](#); [Zhou et al., 2019](#)). To better constrain the effects of these changed aerosol properties, collection and analysis of in-situ, well-aged aerosols is required.

One way to ensure that collected aerosols are well-aged is to collect them at remote locations: remote locations with little to no nascent aerosol production ensure that the aerosols collected must have traveled and aged. To further ensure that the aerosols collected are aged and not from nearby sources, the collection of aerosols in the free troposphere instead of the PBL is often employed. One such way of doing this is by collecting at remote, high-altitude sites, usually mountaintop observatories; an alternative is collection by flights through the free troposphere, but these are limited in their collection time and are often more expensive ([Zhou et al., 2019](#)). One such mountaintop site is the Observatório da Montanha do Pico (OMP), located in the Northeast Atlantic in the Azores Islands. Periodic collection of aerosol samples, as well as continuous air mass measurements, have been performed, mostly during summertime, at the site for nearly two decades, enabling the study of well-aged aerosols in the Northern hemisphere, particularly from North America.

This paper presents a study of aerosols collected at OMP during June and July of 2015. The paper first discusses the physicochemical properties of seven different aerosol samples, including composition and optical properties, as well as estimates of the aerosol aging time and transport path. Next, a more detailed comparison of the previously mentioned properties between two types of aerosol samples is presented. Finally, the potential radiative forcing is estimated for two different extrema of surface reflectivities for two of the samples.

## 2 Methods

### 2.1 Observatório da Montanha do Pico (OMP)

Established in 2001 to observe long-range transport of atmospheric components, the Observatório da Montanha do Pico (OMP) (Pico Mountain Observatory) in the Azores in the northeast Atlantic (38.47° N, 28.40° W), offers the opportunity to collect and analyze well-aged aerosols. OMP is located 2225 m a.s.l in the summit caldera of the Pico Volcano, by far the highest orographic point in a radius of several hundreds of kilometers ([Honrath et al., 2004](#)). Due to the elevation and location, OMP is often in the free troposphere during summer with little influence from the local marine boundary layer (MBL) and from local sources, and therefore, little affected by nascent aerosols. OMP had been operating mostly during summer seasons from 2001 until 2018. Instrumentation at OMP continuously recorded information about the air masses that reached the site. Over the years, in addition to monitors for gaseous species, a meteorological station, and a low-cost custom pyranometer, the site has been equipped with some aerosol instrumentation including a nephelometer, an aethalometer, and a two-channel optical particle counter. Periodically, samples of atmospheric particles have also been collected on various substrates using impactors and aspirators. These samples have been used to analyze the aerosol physicochemical properties, as will be discussed later.

### 2.2 Optical and Radiative Properties

When radiation strikes an aerosol particle, electric charges in the particle are excited, which then either mostly elastically re-radiate (scatter) or absorb the electromagnetic energy. The scattering and absorption cross-sections depend on the wavelength of the radiation, the particles' size, and the refractive index, often normalized by the medium (in this case, air), and their shape and structure ([Seinfeld & Pandis, 2016](#)). The re-radiated light can be scattered in all directions evenly (isotropic), or with a preference for forward- or backward-scattering depending on the previously mentioned radiation and aerosol properties. The sum of the total scattered and absorbed light is called extinction. The total scattering of an ensemble of particles can be measured by collecting the scattered light over a wide-angle ([Uin, 2016](#)), while the absorption can be estimated by sampling particles on a filter and measuring the attenuation of light ([Hansen, 2005](#)).

At OMP, the total scattering and backscattering coefficients (all scattering in the backward hemisphere) of the aerosols were recorded using the integrating nephelometer (Aurora3000, Ecotech) operating at three different wavelengths: 450 nm, 525 nm, and 635 nm. The instrument also recorded sampled air and instrumental temperatures, as well as sampled air pressure and humidity inside the optical cavity. The aerosol absorption coefficients, equivalent black carbon mass concentration, and the concentration of iron-containing mineral dust particles were estimated using a seven-wavelength (370 nm, 470 nm, 520 nm, 590 nm, 660 nm, 880 nm, and 950 nm) aethalometer (AE31 Aethalometer, Magee Scientific).

The scattering and absorption coefficients measured by the aethalometer and nephelometer are extensive quantities, which depend on the particle optical properties, as

well as on their number concentrations. However, from these extensive quantities, several intensive parameters can be calculated. These parameters are independent of the aerosol concentration and allow us to better understand how the aerosol particles interact with radiation. In other words, ratios of the optical coefficients can provide more intuitive and dimensionless quantities to examine and better understand the optical properties of the aerosol. One such ratio is the single scatter albedo,  $\omega$ , which is the ratio of the total scattering to the extinction ([Seinfeld & Pandis, 2016](#)):

$$\omega = \frac{C_{Scat}}{C_{Ext}} \quad \text{Eq. 1}$$

The value of  $\omega$  ranges between  $> 0$  and 1, with low values meaning there is little contribution to extinction by scattering, and 1 meaning only scattering and no absorption occurs. Typical atmospheric values of  $\omega$  over visible wavelengths range between 0.85 and 0.98 in rural or remote regions, with lower values in more polluted areas ([Andrews et al., 2017](#)).

Another useful ratio is the Ångström exponent,  $\alpha$ . The Ångström exponent was originally proposed as an empirical parameter to describe the spectral dependence of the light extinction, scattering, or absorption of atmospheric aerosols, by approximating this dependence with a power law. Ångström exponents are related to the physical and chemical properties of the individual particles. For example, the total scattering Ångström exponent (SAE) is strongly related to the aerosol size distribution ([Kaskaoutis et al., 2007](#)), while the absorption Ångström exponent can provide insight into the aerosol composition. The scattering Ångström exponent ( $\alpha_{Scat}$ ) is calculated as:

$$\alpha_{Scat} = -\frac{\ln(C_{Scat}(\lambda_1)/C_{Scat}(\lambda_2))}{\ln(\lambda_1/\lambda_2)} \quad \text{Eq. 2}$$

where  $C_{Scat}$  is the measured scattering coefficient and  $\lambda_{1,2}$  are two wavelengths at which the scattering is measured ([Liu et al., 2018](#)). Larger values of  $\alpha_{Scat}$  ( $> 1$ ) correspond to smaller aerosol particles in a distribution, while smaller values of  $\alpha_{Scat}$  ( $\leq 1$ ) correspond to larger aerosol particles. A similar equation can be written for the absorption Ångström exponent ( $\alpha_{Abs}$ ), with the measured absorption coefficients,  $C_{Abs}$ , in place of the measured scattering coefficients. The  $\alpha_{Abs}$  can provide information on the aerosol composition, particularly that of black carbon, brown carbon, and iron-containing mineral dust ([Fialho et al., 2006](#); [Fialho et al., 2005](#); [Pavese et al., 2012](#)).

Knowing the radiative forcing of aerosols is important for understanding their roles in the planetary radiative balance and hence in the climate. Estimating the aerosol radiative forcing requires knowing how different aerosols scatter and absorb radiation. An analytical expression for the aerosol spectral radiative forcing is given as ([Bhandari et al., 2019](#); [Chylek & Wong, 1995](#); [Lenoble et al., 1982](#); [Moosmüller & Ogren, 2017](#)):

$$SRF(\lambda) \equiv -\frac{1}{2} \frac{\Delta S(\lambda)}{\Delta \lambda} T_{atm}^2 (1 - A_{cld}) \tau \left[ \bar{\beta}(\lambda) \omega(\lambda) (1 - R_{surf})^2 - 2(1 - \omega(\lambda)) R_{surf} \right] \quad \text{Eq. 3}$$

where  $SRF(\lambda)$  is the spectral radiative forcing,  $\Delta S(\lambda)/\Delta\lambda$  is the spectral solar irradiance,  $T_{atm}$  is the transmittance of the atmosphere above the aerosol layer,  $A_{cld}$  is the fractional cloud cover above the aerosol layer,  $\tau$  is the aerosol optical depth (AOD),  $\bar{\beta}(\lambda)$  is the wavelength dependent average aerosol upscatter fraction for the earth's sunlit hemisphere,  $\omega(\lambda)$  is the wavelength dependent single scattering albedo, and  $R_{surf}$  is the surface reflectance (also termed albedo). The value of the average radiative forcing can be negative (cooling), positive (warming), or zero (no forcing). Considering the limits of  $\omega$ , one can gain an understanding of the effect of aerosol albedo. For  $\omega = 0$ , the average aerosol radiative forcing is positive, indicative of warming, while for  $\omega = 1$ , the forcing is negative, indicative of cooling. While it is nearly impossible to achieve  $\omega = 0$  for an atmospheric particle, it provides a lower mathematical limit.

As a step towards determining the aerosol radiative forcing, the average aerosol upscatter fraction,  $\bar{\beta}$ , needs to be determined. However, to date, there is no method to directly measure it. One parameter that can be directly calculated from the scattering and backscattering is the backscatter fraction,  $b$ , defined as the ratio of the backscattered coefficient ( $S_B$ ) to the total scattering coefficient ( $S_{Total}$ ):

$$b = \frac{S_B}{S_{Total}} \quad \text{Eq. 4}$$

From  $b$ , the asymmetry parameter,  $g$ , can be calculated; while not strictly necessary for determining  $\bar{\beta}$ , it is useful to compare  $g$  to existing published values. The asymmetry parameter can range between -1 and 1, with negative values corresponding to backward scattering, and positive values to forward scattering;  $g = 0$  corresponds to isotropic scattering ([Seinfeld & Pandis, 2016](#)). While it is necessary to know the entire phase function to fully determine  $g$ , some approximations can be made to determine it from  $b$ . The simplest, linear approximation is ([Sagan & Pollack, 1967](#)):

$$g_{lin} = 1 - 2b \quad \text{Eq. 5}$$

However, as a linear approximation, the values of  $g$  are only good near the extremes of  $g = 0$  and  $g = 1$ . Meanwhile, a more accurate relationship applying the Henyey-Greenstein phase function approximation relates  $g$  to  $b$  through an empirical polynomial fit as ([Moosmüller & Ogren, 2017](#)):

$$g_{fit} = -6.347b^3 + 6.906b^2 - 3.859b + 0.9852 \quad \text{Eq. 6}$$

For completeness and comparison, both approximations of the asymmetry parameter are calculated in this paper.  $\bar{\beta}$  can be approximated using a fifth-order polynomial of the backscatter fraction,  $b$ , as ([Moosmüller & Ogren, 2017](#)):

$$\bar{\beta} = 99.69b^5 - 144.6b^4 + 80.44b^3 - 22.05b^2 + 3.73b + 0.018 \quad \text{Eq. 7}$$

It is from here that the spectral radiative forcing can be calculated from Eq. 3. The values of  $\omega$  and  $\bar{\beta}$  were determined using Eq. 1 and Eq. 7 respectively. Meanwhile, the values

for  $T_{atm}$ ,  $A_{cld}$ , and  $R_{surf}$ , were chosen from previous literature, and  $\tau$  was estimated from measurements of the AOD at a nearby site. It should be noted that the wavelength dependence of  $\tau$ ,  $T_{atm}$ , and  $R_{surf}$  were neglected in our calculations. The average spectral solar irradiance at each of the nephelometer wavelength bands was determined by calculating a weighted average of the spectral solar irradiance over the emission range of each nephelometer LED, with the weight being the LED relative spectral power distribution. The nephelometer LED relative spectral power distribution curves are given in Appendix A.3, while the values used in Eq. 3 are given in Appendix A.4.

## 2.3 Aerosol Sampling and Single Particle Analysis

To study the link between aerosol optical and radiative properties and the details of their physical and chemical properties at the single particle level, we also collected particles on substrates for off-line micro-spectroscopic analyses. Samples were collected at OMP in June and July of 2015 to ensure free tropospheric conditions, which are more likely to occur in the summer. Aerosols were collected using a four-stage cascade impactor (MPS-4G1) onto TEM B-film grids (300 mesh, Ted Pella, Inc.) with a flow rate of 6.5 lpm, on stage 3 (50% aerodynamic diameter cutoff of  $> 0.15 \mu\text{m}$ ), and stage 4 (50% cutoff of  $> 0.05 \mu\text{m}$ ).

### 2.3.1 Computer-controlled Scanning Electron Microscopy with Energy Dispersive X-ray Spectrometry

We analyzed the samples using a computer-controlled scanning electron microscope with an energy dispersive X-ray spectrometer (FEI Quanta) (CCSEM-EDX). We analyzed the SEM images to calculate individual particles' shape, morphology, and size (area equivalent diameter). The electron beam of the SEM is used to excite the electrons to a higher energy state, leaving an electron hole; when the electron hole is filled, X-rays are emitted, and the characteristic energy value is used to determine the elemental composition. The X-rays must have sufficient energy to escape the material, so the quantification of elements at the edge of this energy barrier is more uncertain. Using the EDX spectrometer (EDAX, Inc.), the elemental composition of the particles was determined, quantifying 15 elements (C, N, O, Na, Mg, Al, Si, P, S, Cl, K, Ca, Mn, Fe, and Zn). Certain elemental combinations and percentages were associated with certain types of aerosols. We grouped the particles' elemental composition into eight categories: (1) oxygen and carbon (OC), (2) carbon with nitrogen and oxygen (CNO), (3) carbon with nitrogen, oxygen, and sulfur (CNOS), (4) sea salt (Na-rich), (5) sea salt/sulfur (Na-rich with S), (6) dust (Al, Si, Ca, Fe), (6) dust with sulfur (Al, Si, Ca, Fe, S) and (7) other. For the classification scheme, please refer to Appendix A.1.

Correctional procedures using a standard material were performed for C, N, and O, as the EDX analysis is only semi-quantitative due to the physical limitations of the technique. More details about the correction calculations are provided in Appendix A.2. Additionally, C and O contributions from the B-film were removed ([Cheng et al., 2022](#)).

### 2.3.2 Particle Mixing State Index

The mixing state index,  $\chi$ , is a numerical representation of how different (externally mixed) or similar (internally mixed) the particles' elemental composition in the sample is. Values for the mixing state can vary from 0% (completely externally mixed) to 100% (completely internally mixed). The mixing state here only accounts for the general elemental makeup and does not account for morphological differences or chemical formulas or structures.

Following the definitions of [Riemer and West \(2013\)](#), the  $i$ th particle in a sample of  $N$  particles, is made up of  $a$  elements, from one element up to a maximum of  $A$ . The mass of each component in the particle is denoted by:

$$\mu_i^a$$

The mass of each particle, the mass of each element in the population of  $N$ , and the total mass of the ensemble are respectively, as follows:

$$\sum_{a=1}^A \mu_i^a = \mu_i$$

Eq. 8

$$\sum_{i=1}^N \mu_i^a = \mu^a$$

Eq. 9

$$\sum_{a=1}^A \sum_{i=1}^N \mu_i^a = \mu$$

Eq. 10

Mass fractions are then calculated as:

$$p_i^a = \mu_i^a / \mu_i$$

Eq. 11

$$p_i = \mu_i / \mu$$

Eq. 12

$$p^a = \mu^a / \mu$$

Eq. 13

These mass fractions are used to calculate the mixing entropies. The mixing entropy of each particle  $i$ , the average particle ( $\alpha$ ) mixing entropy, and the population bulk ( $\gamma$ ) mixing entropy respectively are:

$$H_i = \sum_{a=1}^A -p_i^a \ln p_i^a$$

Eq. 14

$$H_\alpha = \sum_{i=1}^N p_i H_i$$

Eq. 15

$$H_\gamma = \sum_{a=1}^A p^a \ln p^a$$

Eq. 16

Using the mixing entropies, the diversity of each particle  $i$ , the average particle ( $\alpha$ ) species diversity, and the bulk population ( $\gamma$ ) species diversity can be calculated.

$$D_i = e^{H_i}$$

Eq. 17

$$D_\alpha = e^{H_\alpha}$$

Eq. 18

$$D_\gamma = e^{H_\gamma}$$

Eq. 19

The diversity of each particle is a numerical representation of how many categories make up that aerosol particle. The average particle diversity is the average effective number of species in each particle in the sample. The bulk population diversity is the effective number of species in the population; the population, in this case, refers to each analyzed sample.

It is from here that the value of the mixing state index can be found using the average particle species diversity and bulk population species diversity.

$$\chi = \frac{D_a - 1}{D_\gamma - 1} \quad \text{Eq. 20}$$

A graphical representation of the mixing state is given in Figure 1. Values of  $\chi$  below 50% represent externally mixed particles in a sample while values above 50% are internally mixed. Pure particles ( $\chi = 0\%$ ) are made of a single element, equal bulk ( $D_\gamma = \text{max.}$ ) is associated with an even distribution of each species though not necessarily equal in each particle, and identical particles ( $\chi = 100\%$ ) are identical to one another. The majority of atmospheric aerosols fall somewhere in between the extrema, with well-aged aerosols expected to be more internally mixed.

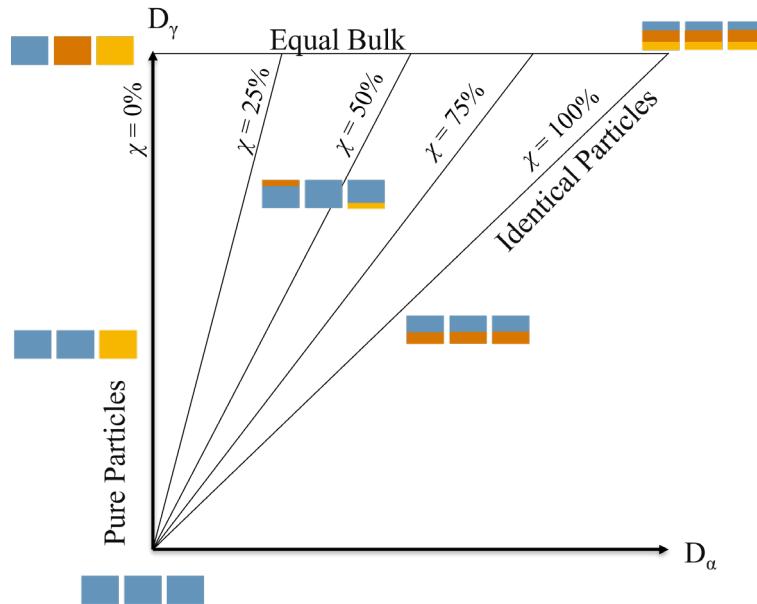


Figure 1: A plot of the mixing state index,  $\chi$ . Lines of constant  $\chi$  are shown in relation to the average particle species diversity,  $D_a$ , and the bulk population species diversity,  $D_\gamma$ . Pure particles are made of a single element, equal bulk is associated with an even distribution of each species, and identical particles are identical to one another. The figure is based on Fig. 2 of [Riemer and West \(2013\)](#).

## 2.4 Particle Concentration and Meteorological Parameters

Aerosol number concentrations were measured using a GT-521S MetOne two-channel laser optical particle counter. Channel One had a 50% size cut of 0.3 microns up to 5 microns and Channel Two had a 50% size cut of 0.4 microns up to 5 microns.

Meteorological data were collected at OMP using a Vantage Pro2 (Davis) station. Recorded data included relative humidity, pressure, temperature, solar radiation, and wind speed. A low-cost custom pyranometer<sup>1</sup> was also deployed and is used here to determine the cloudiness at the site during some of the sampling times.

## 2.5 FLEXible PARTicle Dispersion Model

The transport pattern, source, and age of the air masses were studied using the FLEXible PARTicle (FLEXPART) model, a Lagrangian particle dispersion model ([Stohl et al., 2005](#)). The model simulates the transport and diffusion of small air parcels by integrating matrices of residence time over both time and altitude, while also predicting removal through wet and dry deposition. These air parcels contain the aerosols being transported to OMP. FLEXPART can be used either forward or backward in time, with the latter option being used in this paper ([Stohl et al., 2005](#)).

A ten-year archive of transport trajectories was formed for OMP, giving the transport pattern for our samples. Using carbon monoxide (CO) inventories from the Emissions Database for Global Atmospheric Research and the Global Fire Emissions Database, CO contributions from anthropogenic and wildfire sources can be estimated ([Zhang et al., 2017](#); [Zhang et al., 2014](#)). In addition, the CO transport time is averaged to estimate the age of the air mass.

---

<sup>1</sup> (<https://instesre.org/construction/pyranometer/pyranometer.htm>)

### 3 Results and Discussion

#### 3.1 Optical and Radiative Properties

A summary of the optical and radiative properties for each sample is given in Table 1. The scattering coefficients,  $C_{Scat}$ , and absorption coefficients,  $C_{Abs}$ , in units of inverse megameters ( $Mm^{-1}$ ), for the three wavelengths of the nephelometer are given, along with their respective standard errors. The scattering Ångström exponents are calculated for three different wavelength pairs as indicated by the subscripts ( $\alpha_{Scat450-635}$ ,  $\alpha_{Scat525-635}$ , and  $\alpha_{Scat525-635}$ ), with a similar structure for the absorption Ångström exponents. An average of the three scattering ratios is given as  $\alpha_{Avg}$ , while  $\alpha_{Fit}$  is the exponent in a power-law fit found using all three scattering wavelengths simultaneously. Additionally, the backscatter fraction,  $b$ , the single scatter albedo,  $\omega$ , and the asymmetry parameter,  $g$ , and the average aerosol upscatter fraction,  $\bar{\beta}$ , are given only for samples S3 and S5-S7, due to instrument issues at the time S1 and S2 were collected, and due to signals below the detection limit for S4. Errors for calculated values are determined using error propagation in quadrature.

Table 1: Optical properties for the seven samples. The scattering coefficients, as well as the scattering Ångström exponents, absorption coefficients, absorption Ångström exponents, backscatter fraction, single scatter albedo, asymmetry parameter, and average upscatter fraction are presented, along with their standard (or propagated) errors. Parameters  $b$ ,  $g$ , and  $\bar{\beta}$  are not available for three of the sample times due to either instrumental issues or signal below the detection limit.

<i>Sample</i>	<i>S1</i> 6/13/15	<i>S2</i> 6/20/15	<i>S3</i> 6/26/15	<i>S4</i> 7/3/15	<i>S5</i> 7/10/15	<i>S6</i> 7/19/15	<i>S7</i> 7/26/15
$C_{Scat-635}$ [ $Mm^{-1}$ ]	$1.0 \pm 0.3$	$6.7 \pm 0.2$	$4.1 \pm 0.3$	$0.33 \pm 0.03$	$5.1 \pm 0.1$	$3.8 \pm 0.2$	$2.6 \pm 0.1$
$C_{Scat-525}$ [ $Mm^{-1}$ ]	$2.5 \pm 0.3$	$7.6 \pm 0.3$	$7.5 \pm 0.5$	$0.71 \pm 0.05$	$9.6 \pm 0.2$	$3.2 \pm 0.1$	$3.4 \pm 0.1$
$C_{Scat-450}$ [ $Mm^{-1}$ ]	$3.4 \pm 0.5$	$9.4 \pm 0.2$	$10.4 \pm 0.8$	$0.94 \pm 0.06$	$13.3 \pm 0.3$	$3.3 \pm 0.1$	$4.3 \pm 0.2$
$\alpha_{Scat450-525}$	$2.0 \pm 1.3$	$1.4 \pm 0.3$	$2.1 \pm 0.7$	$1.8 \pm 0.6$	$2.1 \pm 0.2$	$0.3 \pm 0.4$	$1.6 \pm 0.3$
$\alpha_{Scat450-635}$	$3.5 \pm 0.9$	$1.0 \pm 0.1$	$2.7 \pm 0.3$	$3.1 \pm 0.3$	$2.78 \pm 0.08$	$-0.4 \pm 0.2$	$1.4 \pm 0.2$
$\alpha_{Scat525-635}$	$4.7 \pm 1.6$	$0.7 \pm 0.3$	$3.1 \pm 0.5$	$4.1 \pm 0.6$	$3.4 \pm 0.1$	$-1.0 \pm 0.3$	$1.3 \pm 0.3$
$\alpha_{Avg}$	$3.4 \pm 1.3$	$1.0 \pm 0.2$	$2.6 \pm 0.5$	$3.0 \pm 0.5$	$2.7 \pm 0.1$	$-0.4 \pm 0.3$	$1.4 \pm 0.3$
$\alpha_{Fit}$	$3.5 \pm 0.7$	$1.0 \pm 0.2$	$2.7 \pm 0.3$	$3.1 \pm 0.6$	$2.8 \pm 0.4$	$-0.4 \pm 0.4$	$1.4 \pm 0.1$
$C_{Abs-635}$ [ $Mm^{-1}$ ]	$1.0 \pm 0.4$			$0.08 \pm 0.02$	$0.40 \pm 0.05$		$0.23 \pm 0.05$
$C_{Abs-525}$ [ $Mm^{-1}$ ]	$0.4 \pm 0.3$			$0.09 \pm 0.03$	$0.52 \pm 0.04$		$0.26 \pm 0.03$
$C_{Abs-450}$ [ $Mm^{-1}$ ]	$0.4 \pm 0.4$			$0.11 \pm 0.02$	$0.57 \pm 0.04$		$0.29 \pm 0.03$
$\alpha_{Abs450-525}$					$0.5 \pm 0.7$		
$\alpha_{Abs450-635}$					$1.0 \pm 0.4$		
$\alpha_{Abs525-635}$					$1.4 \pm 0.8$		

$b_{635}$	$0.23 \pm$	$0.24 \pm$	$0.17 \pm$	$0.09 \pm$
	0.02	0.01	0.01	0.01
$b_{525}$	$0.11 \pm$	$0.090 \pm$	$0.08 \pm$	$0.13 \pm$
	0.01	0.005	0.01	0.01
$b_{450}$	$0.12 \pm$	$0.098 \pm$	$0.12 \pm$	$0.09 \pm$
	0.01	0.005	0.01	0.01
$\omega_{635}$		$0.931 \pm$		$0.92 \pm$
		0.009		0.01
$\omega_{525}$		$0.952 \pm$		$0.950 \pm$
		0.004		0.006
$\omega_{450}$		$0.962 \pm$		$0.944 \pm$
		0.002		0.005
$g_{lin-635}$	$0.53 \pm$	$0.53 \pm$	$0.67 \pm$	$0.81 \pm$
	0.04	0.02	0.02	0.02
$g_{lin-525}$	$0.79 \pm$	$0.82 \pm$	$0.83 \pm$	$0.74 \pm$
	0.02	0.01	0.02	0.02
$g_{lin-450}$	$0.76 \pm$	$0.80 \pm$	$0.76 \pm$	$0.82 \pm$
	0.02	0.01	0.02	0.02
$g_{cube-635}$	$0.38 \pm$	$0.38 \pm$	$0.50 \pm$	$0.68 \pm$
	0.04	0.02	0.02	0.02
$g_{cube-525}$	$0.64 \pm$	$0.69 \pm$	$0.71 \pm$	$0.59 \pm$
	0.03	0.01	0.03	0.02
$g_{cube-450}$	$0.61 \pm$	$0.67 \pm$	$0.61 \pm$	$0.69 \pm$
	0.03	0.01	0.03	0.02
$\bar{\beta}_{635}$	$0.35 \pm$	$0.35 \pm$	$0.30 \pm$	$0.23 \pm$
	0.02	0.01	0.01	0.01
$\bar{\beta}_{525}$	$0.25 \pm$	$0.22 \pm$	$0.21 \pm$	$0.27 \pm$
	0.01	0.01	0.02	0.01
$\bar{\beta}_{450}$	$0.26 \pm$	$0.24 \pm$	$0.26 \pm$	$0.23 \pm$
	0.01	0.01	0.01	0.01

The scattering coefficients at OMP are relatively low, compared to values of several dozen  $\text{Mm}^{-1}$  typical in moderately polluted areas, and hundreds of  $\text{Mm}^{-1}$  seen in highly polluted environments ([Di Biagio et al., 2016](#); [Yu et al., 2019](#)). This is consistent with the expectation that OMP was in the free and remote troposphere during these sampling times, as the remote free troposphere is typically less polluted than the MBL. Higher ( $> 1$ ) values of the SAE for samples S1, S3, S4, S5 and S7 indicate the dominance of smaller particles in the sample, while the lower values ( $\leq 1$ ) for samples S2 and S6 indicate larger particles are present in the sample, often associated with mineral dust ([Redmond et al., 2010](#)).

The values of  $b$ ,  $g_{lin}$ , and  $g_{cube}$ , generally fall within the range discussed in [Andrews et al. \(2006\)](#), though lower values of 0.38 for  $g_{cube}$  for samples S3 and S5 occur, as well as higher values of  $> 0.71$  for  $g_{lin}$  for samples S3, S5, S6 and S7. The general overestimation of  $g_{lin}$  highlights the shortcomings of the linear approximation for the asymmetry parameter for realistic atmospheric values as discussed in [Moosmüller and Ogren \(2017\)](#).

The values of  $\bar{\beta}$  fall between 0.21 and 0.35, values which are within the range of previous literature results ([Nemesure et al., 1995](#); [Wiscombe & Grams, 1976](#)).

## 3.2 Single Particle Analysis

The sampling information, elemental composition, and average diameter for the seven samples are summarized in Table 2. Excluding sample S7, all samples were collected in the afternoon or evening, with sampling times from around 30 minutes to around four hours. All samples contain a significant number of carbonaceous particles (OC+CNO+CNOS), with mineral dust the next most common, followed by sea salt and sea salt/sulfur. The average area equivalent diameters (AED) of samples S2 and S4 are smaller than the other samples, while sample S5 has the largest average AED.

Table 2: A summary of the seven samples including collection date and time, chemical composition, and the average diameter. All samples are predominantly carbonaceous.

<i>Sample</i>	<i>S1</i>	<i>S2</i>	<i>S3</i>	<i>S4</i>	<i>S5</i>	<i>S6</i>	<i>S7</i>
<i>Date</i>	6/13/15	6/20/15	6/26/15	7/3/15	7/10/15	7/19/15	7/26/15
<i>Start Time</i>	15:32	15:15	15:22	15:20	17:10	13:38	Between 8:10 and 8:40
<i>End Time</i>	16:37	15:50	17:58	19:09	18:40	17:51	15:00
<i>OC (%)</i>	86.7	79.8	50.0	77.6	88.9	40.3	56.4
<i>CNO (%)</i>	0.0	0.0	0.0	0.0	0.2	0.0	0.0
<i>CNOS (%)</i>	3.7	12.1	27.8	12.2	3.3	12.7	22.6
<i>Sea salt (%)</i>	2.9	2.5	0.2	1.8	0.9	0.3	1.3
<i>Sea salt/Sulfur (%)</i>	1.6	2.7	4.8	6.4	5.9	5.9	9.0
<i>Dust (%)</i>	4.0	0.9	15.8	1.0	0.4	39.0	9.0
<i>Dust with Sulfur (%)</i>	0.2	0.4	0.5	0.0	0.1	1.0	0.6
<i>Other (%)</i>	1.0	1.5	1.1	1.0	0.3	0.8	1.1
<i>Average diameter [<math>\mu\text{m}</math>]</i>	0.324	0.195	0.420	0.179	0.466	0.593	0.408

### 3.2.1 CCSEM-EDX

The CCSEM-EDX analysis of the seven samples is shown in Figure 2. The top left plot gives a summary of the composition of all seven samples, while the other plots show the individual normalized composition of each sample, with respect to the area equivalent

diameter of the particles within the sample. As mentioned earlier, all samples are largely made up of carbonaceous aerosols (OC+CNO+CNOS), with a large fraction of the carbonaceous aerosols being made up of OC (oxygen and carbon). Samples S3 and S6 contain a significant fraction of mineral dust and small amounts of mineral dust with sulfur. Samples S3 and S6 also contain larger particles, as shown by the area equivalent diameter range of the two samples compared to the other five samples.

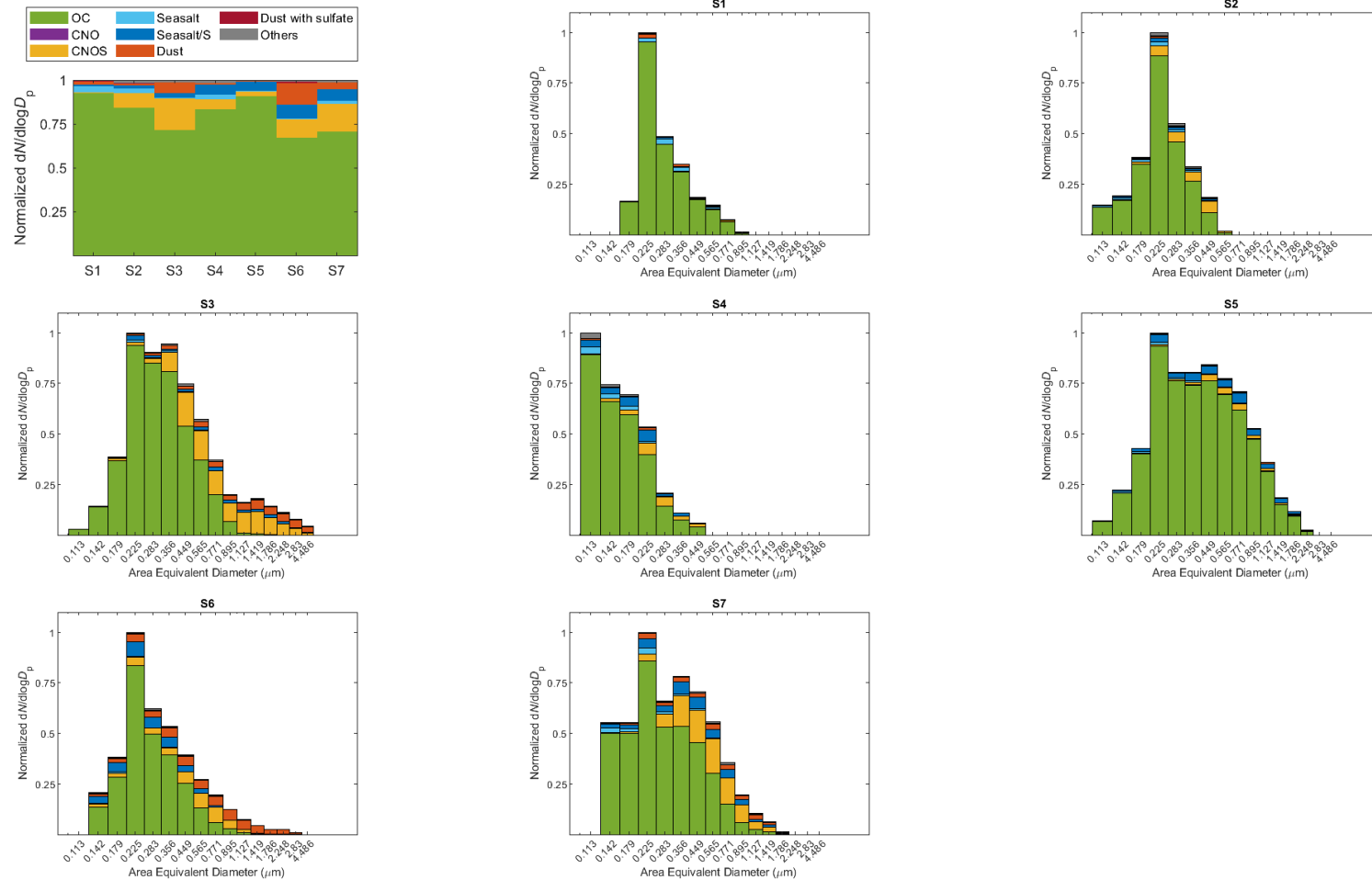


Figure 2: The classified chemical composition of the seven samples. The first figure gives the summary of all the samples, followed by each of the individual samples (as indicated by the label above each plot) plotted against the area equivalent diameter.

### 3.2.2 Mixing State Index

Table 3 lists the average particle species diversity ( $D_\alpha$ ), the bulk population species diversity ( $D_\gamma$ ), and the mixing state index values of each sample. The particles of all the samples are significantly internally mixed, with the lowest mixing state index value,  $\chi$ , being just above 58% (S1) and the highest being nearly 79% (S2 and S5). The average particle species diversity  $D_\alpha$  tends to be close to its maximum value (the bulk population diversity  $D_\gamma$ ) indicating that the particles have similar mass fractions within each sample. The bulk population diversity is relatively low compared to its potential maximum of the total number of elements (in this case,  $D_{\gamma-Max} = 15$ ), which is indicative that while the particles have similar mass fractions, the bulk mass fractions are not equal ([Riemer & West, 2013](#)).

Table 3: Average particle species diversity, bulk population species diversity, and the mixing state index for the seven samples. All samples are internally mixed, with the mixing state index  $\chi$  falling between 58% and 79%.

<i>Sample</i>	$D_\alpha$	$D_\gamma$	<i>Mixing State Index <math>\chi</math></i> (%)
<i>S1</i>	1.2	1.4	58.3
<i>S2</i>	1.2	1.2	78.7
<i>S3</i>	1.4	1.5	74.3
<i>S4</i>	1.4	1.5	73.5
<i>S5</i>	1.5	1.7	78.4
<i>S6</i>	4.0	5.3	69.6
<i>S7</i>	1.8	2.1	73.7

### 3.3 Particle Count and Meteorological Parameters

Table 4 gives the averages for the particle count, as well as the ratio  $(C_1-C_2)/C_1$ , and the averages for the meteorological measurements of pressure, temperature, relative humidity, and wind speed. The ratio  $(C_1-C_2)/C_1$  is the difference of the particle counts in the two size channels divided by the count in the first channel. Larger values for the ratio indicate an abundance of smaller particles, while lower values indicate the presence of larger particles. The  $(C_1-C_2)/C_1$  ratio for all sample periods for which counts were available, excluding S6 are 0.69 or greater, indicating an abundance of small particles in agreement with the higher SAE values in section 3.1. The pressure and temperature for all samples differed slightly, while samples were collected at humidity conditions that varied over a wide range. The average wind speed tended to be around 2 mph for samples S1-S5, while samples S6 and S7 had higher wind speeds around 5 and 4 mph, respectively.

Table 4: Average particle count and meteorological data, plus their respective standard deviations for the seven samples. Samples S2 and S3 do not have recorded particle count data.

<i>Sample</i>	<i>S1</i>	<i>S2</i>	<i>S3</i>	<i>S4</i>	<i>S5</i>	<i>S6</i>	<i>S7</i>
<i>Channel 1 Count</i>	2410 ± 1240			467 ± 199	13303 ± 1174	1664 ± 431	4256 ± 1333
<i>Channel 2 Count</i>	654 ± 323			140 ± 60	3582 ± 364	830 ± 304	1231 ± 348
<i>Ratio (C<sub>1</sub>-C<sub>2</sub>)/C<sub>1</sub></i>	0.73 ± 0.01			0.69 ± 0.02	0.731 ± 0.005	0.52 ± 0.07	0.70 ± 0.02
<i>Pressure (hPa)</i>	788.3 ± 0.1	792.3 ± 0.1	791.5 ± 0.3	787.5 ± 0.2	792.26 ± 0.03	785.3 ± 0.6	792.1 ± 0.6
<i>Temperature (°C)</i>	10.2 ± 0.3	12.3 ± 0.1	14.1 ± 0.6	7.9 ± 0.3	10.29 ± 0.05	10.7 ± 0.2	11.7 ± 0.6
<i>Relative Humidity (%)</i>	60 ± 10	47.8 ± 2.0	61.4 ± 2.5	67.7 ± 2.6	26.2 ± 0.8	97.4 ± 0.9	50 ± 10
<i>Wind speed (mph)</i>	1.4 ± 0.3	2.0 ± 0.1	2.4 ± 0.7	2.0 ± 0.4	2.7 ± 0.3	5.1 ± 0.5	4.4 ± 0.9

### 3.4 FLEXPART

The retroplume analysis for the periods during which the seven samples were collected is shown in Figure 3. Plotted are the vertically integrated weighted residence times. The integrated residence times are normalized to the maximum integrated residence time (100%) on the plot to show the distribution of the air mass. The logscale color bar, therefore, represents the ratio of the location to the maximum integrated residence time (Schum et al., 2018).

The air masses all originated from North America (NA), with contributions from South America, the Arctic, and recirculation over the North Atlantic Ocean. The transport timescale over the North Atlantic varied by sample, with 4, 12, 3, 3, 3, 14, and 14 days for samples S1-S7 respectively. Samples S4 and S5 were affected by air masses from over the Arctic in addition to the NA emissions. Meanwhile, samples S3 and S6 show recirculated air masses from over the tropic dust belt, indicating the likely contribution of transported aged mineral dust to OMP, which is also seen in the dust contribution of the CCSEM-EDX analysis, the low SAE values, and, for S6, the low (C<sub>1</sub>-C<sub>2</sub>)/C<sub>1</sub> ratio from the particle counter.

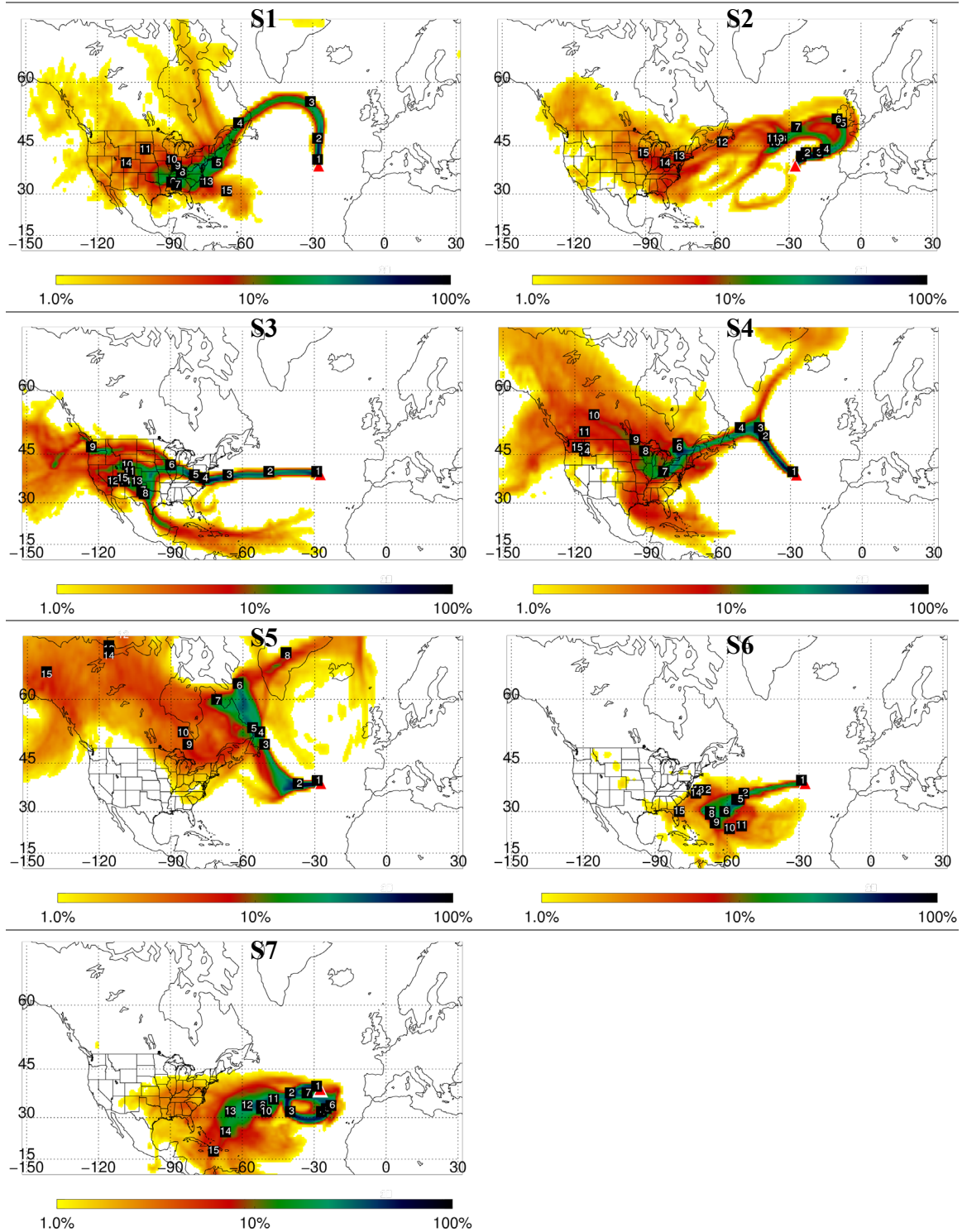


Figure 3: FLEXPART retrorplumes for seven samples collected in June and July of 2015. All the samples from S1 to S5 are affected by transport largely from the North American continent, while the last two, S6 and S7, show some transport from North America, but also some recirculation over the Atlantic.

Figure 4 shows CO tracer simulations for June and July 2015. All samples contain significant CO contributions from anthropogenic NA emissions. Additionally, samples S1, S2, S4, S5, S6, and S7 show CO contributions from wildfire emissions. Samples S2, S5, and S6 show significant levels of CO from wildfire (>30% of total tracer emissions), indicating biomass burning events (~38%, >90%, ~50% of the total, respectively).

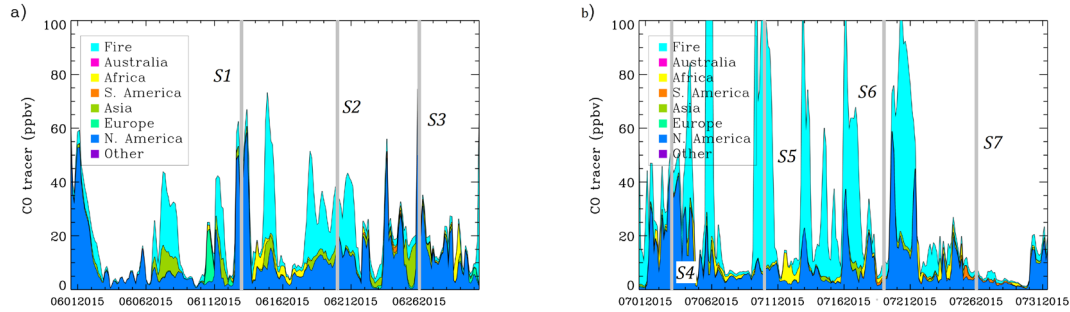


Figure 4: FLEXPART CO tracer simulations for (a) June and (b) July of 2015. All samples show CO contributions from anthropogenic North American emissions, and samples S2, S5, and S6 were affected by CO wildfire emissions consistent with biomass burning.

### 3.5 Comparison of Samples S5 and S6

To investigate different kinds of air masses that reached OMP, samples S5 and S6 will be discussed in more detail to compare between two types of events (biomass burning vs mineral dust), as well as two different transport time scales over the North Atlantic (3 vs 14 days).

Figure 5 shows the solar irradiance during the day for samples S5 and S6, while the boxed times are during the impactor collection time. Lower values and a less smooth diurnal curve for S6 indicate the presence of clouds above. Additionally, the high relative humidity for this sample (97.4%) suggests the sampling occurred in or near clouds.

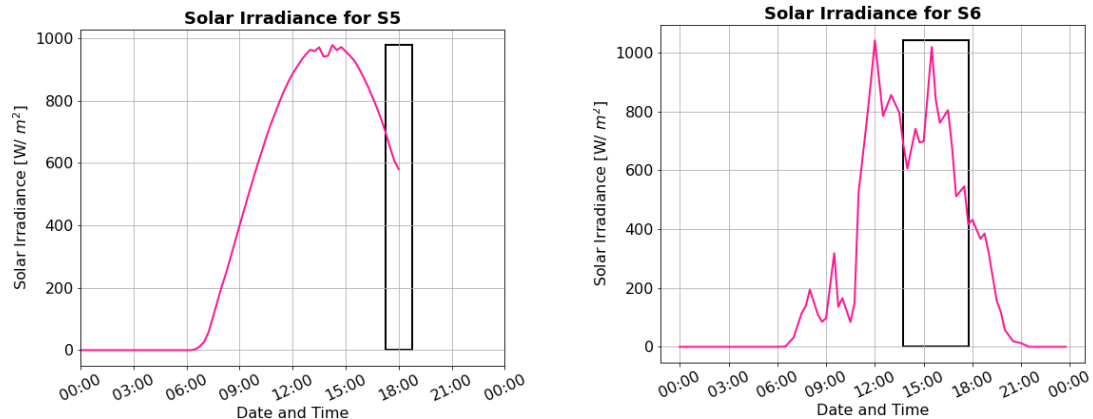
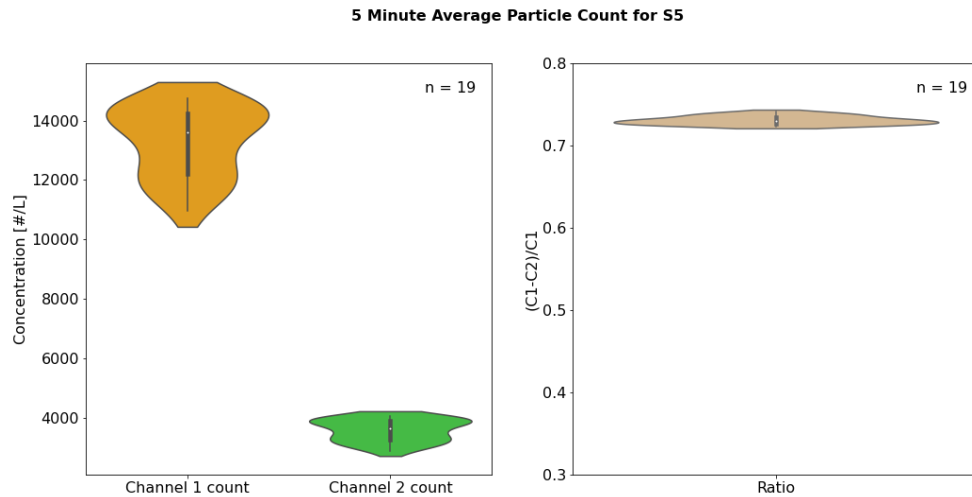


Figure 5: The solar irradiance for samples S5 (left) and S6 (right). The boxes highlight the impactor collection time. Data for sample S5 ends at 18:00 while the impactor

collection time continues through to 18:40. The fluctuations in the solar radiation for sample S6 suggest cloud above.

Aerosol particle count violin plots are given for samples S5 and S6 in Figure 6. As mentioned before, channel 1 is representative of smaller particles down to 0.3  $\mu\text{m}$ , while channel 2 is representative of larger particles, above 0.4  $\mu\text{m}$ . For sample S5 there is a high concentration of smaller particles, with channel 1 having approximately three times as many particles as channel 2. This is further seen in the ratio violin plot, where there is a narrow ratio range, centered around 0.73, indicating a significant presence of small particles to large particles. As biomass burning aerosols tend to be small, this agrees with the FLEXPART analysis which shows dominating wildfire contributions from North America ([Seinfeld & Pandis, 2016](#)).

For sample S6, there is still a greater concentration of small to large particles, albeit less marked than S5. The ratio is also lower and with a wider range, centered around 0.52, indicating a more varied distribution of both small and large particles compared to sample S5. The FLEXPART analysis is also consistent with a combination of both small and large particles, considering that the transport path and CO tracer suggest contributions from small biomass burning particles as well as larger mineral dust particles ([Mahowald et al., 2014](#); [Seinfeld & Pandis, 2016](#)).



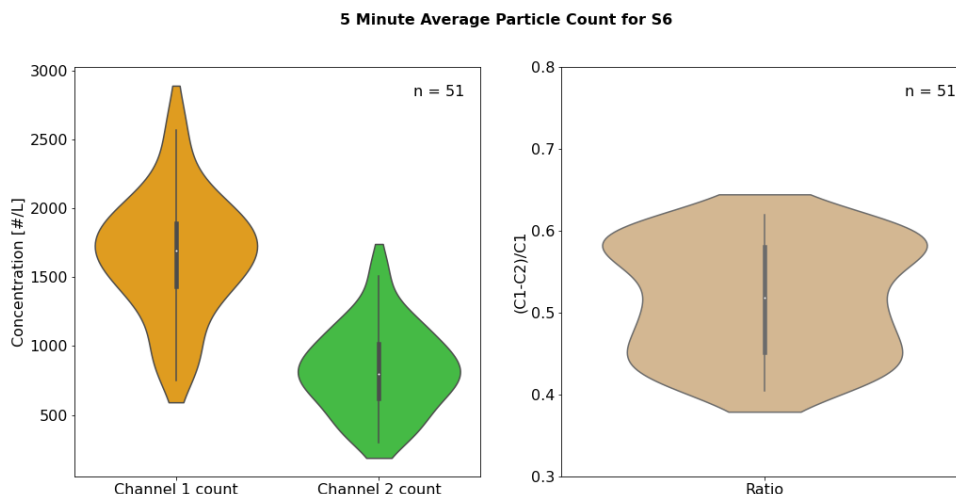


Figure 6: The particle counts for channels 1 and 2, as well as the ratio of the channels  $(\text{Channel}_1 - \text{Channel}_2) / \text{Channel}_1$  for S5 (top) and S6 (bottom). The higher the ratio, the greater the concentration of small particles.

Referring to Figure 2 for the CCSEM-EDX analysis, sample S5 shows predominantly carbonaceous particles, particularly oxygen and carbon (O+C). Additionally, most diameter bins have contributions from sea salt/sulfur. While a greater number of bins contribute to the normalized contribution, most particles are under  $1 \mu\text{m}$ . Sample S6 also contains predominantly carbonaceous particles for most diameter bins, with the largest bins containing only dust.

Time series of the measured scattering and backscattering coefficients for samples S5 and S6 are given in Figure 7. The plots on the left represent the entire sampling day, while the plots on the right are over the sample collection timeframe. The scattering coefficients over the sampling time, as well as over the entire day, for S5 have a strong wavelength dependence as also indicated by the scattering Ångström exponent values reported in Table 1 and Figure 8. This wavelength dependence is also consistent with small biomass burning particles. Meanwhile, the scattering coefficients over the sampling day and time for S6 are considerably less dependent on wavelength, consistent with the presence of larger mineral dust particles.

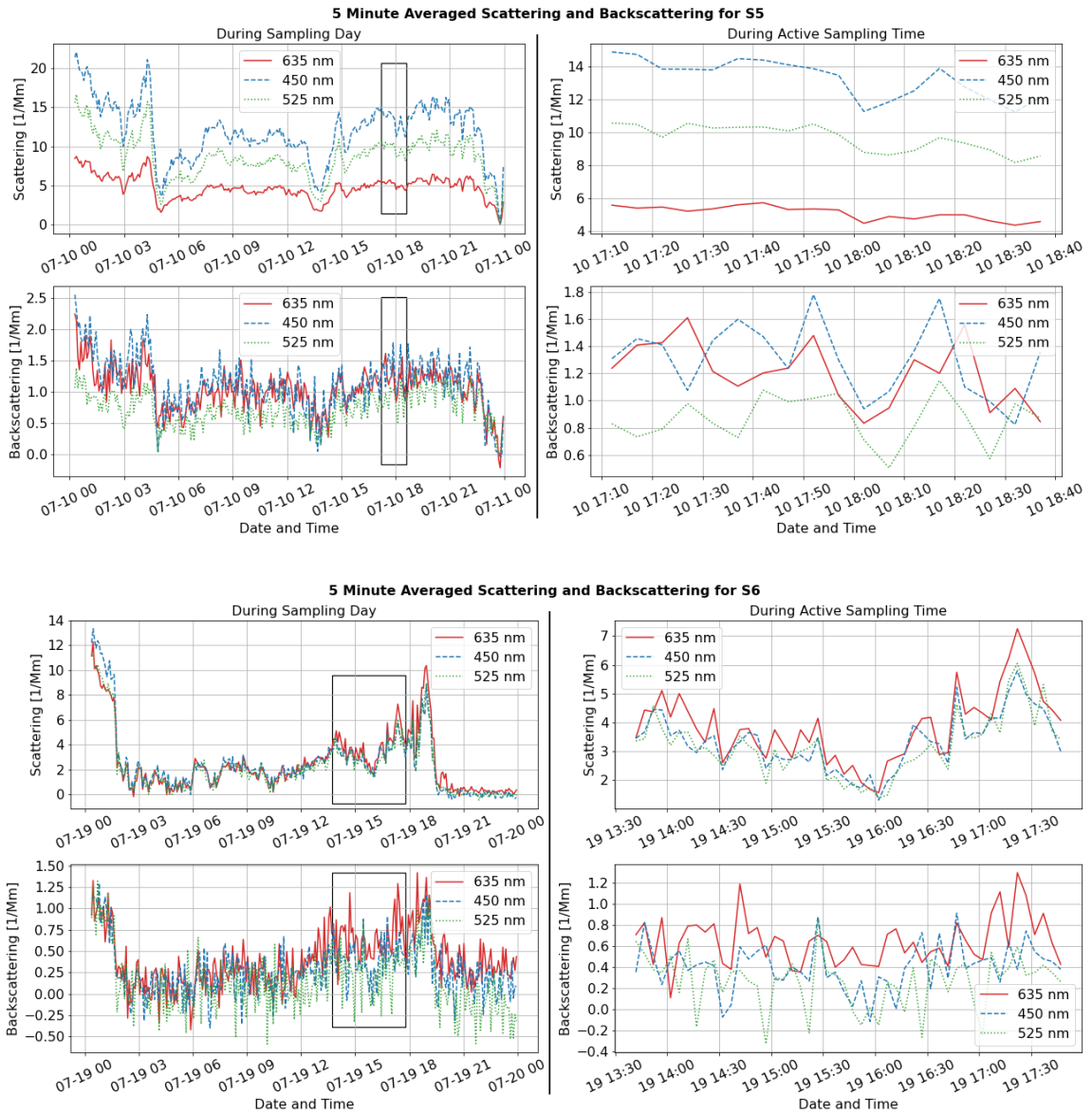


Figure 7: Measured scattering and backscattering coefficients for samples S5 (top) and S6 (bottom). Scattering coefficients for sample S5 show strong wavelength dependence, while for sample S6, there is little wavelength dependence.

Plots of the scattering Ångström exponents for three wavelength ratios during the sampling time for S5 and S6 are shown in Figure 8. For sample S5, all Ångström exponents are above 1, consistent with the presence of small particles in the sample throughout the sampling period. Meanwhile, the scattering Ångström exponents for sample S5 tend to fluctuate around zero, indicative of the presence of large mineral dust particles.

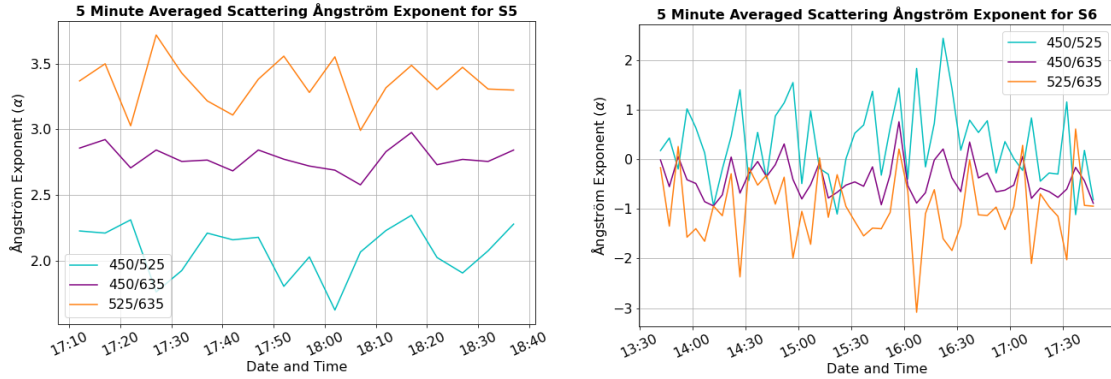


Figure 8: The 5-minute averaged scattering Ångström exponents for samples S5 (right) and S6 (left). Three wavelength ratios are presented (450 525, 450 635, and 525 635).

As absorption coefficients and single scatter albedo values were only available for samples S5 and S7, the average aerosol spectral radiative forcings (Eq. 3) at the three nephelometer wavelengths were calculated for these two samples, and the results are presented in Table 5. The calculation was performed for two scenarios (1) assuming the aerosol to be above clear sky ocean, and (2) assuming the aerosol to be above clouds to represent two extremes in surface reflectivity. Having the ocean as the surface below results in potential negative radiative forcing, or cooling for all three wavelengths for both samples. For the case of aerosol above a low-level cloud layer, the potential radiative forcing is positive for both samples, indicative of warming.

Table 5: Aerosol spectral radiative forcing for samples S5 and S7 above clear sky ocean and above cloud. Negative forcing above the ocean indicates potential cooling, while positive forcing above clouds indicates potential warming.

	<i>Spectral Radiative Forcing (<math>W m^{-2} nm^{-1}</math>)</i>	<i>Above Ocean</i>	<i>Above Cloud</i>
<b>S5</b>	<i>SRF(635 nm)</i>	$(-5.7 \pm 0.2) * 10^{-3}$	$(2.0 \pm 0.3) * 10^{-3}$
	<i>SRF(525 nm)</i>	$(-4.2 \pm 0.1) * 10^{-3}$	$(1.6 \pm 0.1) * 10^{-3}$
	<i>SRF(450 nm)</i>	$(-4.8 \pm 0.1) * 10^{-3}$	$(1.2 \pm 0.1) * 10^{-3}$
<b>S7</b>	<i>SRF(635 nm)</i>	$(-3.6 \pm 0.2) * 10^{-3}$	$(2.5 \pm 0.4) * 10^{-3}$
	<i>SRF(525 nm)</i>	$(-5.1 \pm 0.2) * 10^{-3}$	$(1.6 \pm 0.2) * 10^{-3}$
	<i>SRF(450 nm)</i>	$(-4.4 \pm 0.2) * 10^{-3}$	$(2.0 \pm 0.2) * 10^{-3}$

The difference between ocean and cloud being cooling and warming respectively stems from the relative surface to aerosol albedo differences. Aerosol over clear sky ocean increases the overall albedo, causing a cooling effect as light is more effectively scattered, while aerosol over low clouds tends to decrease the overall albedo if the aerosol is absorbing (Bellouin et al., 2020). As mentioned above, the surface reflectivities are set as two extreme ends, so these values are closer to bounds on the aerosol spectral radiative forcing, with a value between the two being the true aerosol spectral radiative forcing. To get the full radiative forcing effect, the forcing would need to be integrated over the entire solar spectrum. Additionally, these values are from measurements taken

over the course of hours in a local region, so while these values are useful for boundaries and understanding part of the well-aged aerosol-radiation interactions (ARI), further work would need to be done to understand the role of these interactions on a global scale. Indeed, the fact that the true value of the ARI for two samples in the visible wavelength range just for OMP lies between positive and negative values highlights the uncertainty in whether aerosols contribute to overall warming or cooling of the atmosphere.

## 4 Conclusion

In this thesis, I discussed seven different aerosol samples collected at OMP during June and July 2015. The aerosol optical and physicochemical properties were analyzed, as well as the transport pattern and time of the air masses carrying the aerosols. The samples were found to have low scattering coefficients, consistent with the site being in the remote free troposphere. High SAE values for three samples indicated smaller particles, while lower SAE values indicated larger particles for two of the samples. These values, along with the particle counts at two size channels, and average area equivalent diameters of collected samples indicated two main types of particles were transported through the air masses that reached OMP, biomass burning and mineral dust.

The CCSEM-EDX for all samples contained large numbers of carbonaceous particles, with smaller number contributions from dust and sea salt/sulfur for some of the samples. All samples showed air mass transport from North America, with smaller contributions from South America, the Arctic, and recirculation over the Atlantic Ocean in some of the samples. Additionally, all samples were significantly internally mixed, with values between 58% and 79%, as expected of well-aged aerosols. The single particle analysis supports what was seen in the optical properties, with both smaller carbonaceous particles and larger mineral dust and sea salt particles making up the composition of the samples.

Two samples, S5 and S6, were looked at in more detail to compare between two types of dominant particle types, S5 being more affected by biomass burning, and S6 more affected by mineral dust aerosols. Additionally, the transport time over the Atlantic Ocean varied greatly between the two samples (3 vs. 14 days, respectively). It was found that sample S5 had smaller particles, scattering with larger wavelength dependence, and a slightly greater upscatter fraction  $\bar{\beta}$ . Meanwhile, sample S6 had larger particles, scattering with little wavelength dependence, and a slightly lower upward scatter fraction  $\bar{\beta}$ .

Finally, the aerosol spectral radiative forcing was calculated for samples S5 and S7, for two different surface reflectivities, and the three wavelengths measured by the nephelometer. Two different outcomes resulted depending on where in the atmosphere the aerosols resided, with cooling observed for the aerosol over the clear sky ocean and warming for the aerosol above clouds. The difference in forcing, for both samples, highlights the need to perform further work towards understanding the role of aerosols and radiation in the atmosphere.

## 5 References

- Andrews, E., Ogren, J. A., Kinne, S., & Samsel, B. (2017). Comparison of AOD, AAOD and column single scattering albedo from AERONET retrievals and in situ profiling measurements. *Atmos. Chem. Phys.*, *17*(9), 6041-6072. <https://doi.org/10.5194/acp-17-6041-2017>
- Andrews, E., Sheridan, P. J., Fiebig, M., McComiskey, A., Ogren, J. A., Arnott, P., Covert, D., Elleman, R., Gasparini, R., Collins, D., Jonsson, H., Schmid, B., & Wang, J. (2006). Comparison of methods for deriving aerosol asymmetry parameter [<https://doi.org/10.1029/2004JD005734>]. *Journal of Geophysical Research: Atmospheres*, *111*(D5). <https://doi.org/https://doi.org/10.1029/2004JD005734>
- Bellouin, N., Quaas, J., Gryspeerdt, E., Kinne, S., Stier, P., Watson-Parris, D., Boucher, O., Carslaw, K. S., Christensen, M., Daniau, A. L., Dufresne, J. L., Feingold, G., Fiedler, S., Forster, P., Gettelman, A., Haywood, J. M., Lohmann, U., Malavelle, F., Mauritsen, T., . . . Stevens, B. (2020). Bounding Global Aerosol Radiative Forcing of Climate Change [<https://doi.org/10.1029/2019RG000660>]. *Reviews of Geophysics*, *58*(1), e2019RG000660. <https://doi.org/https://doi.org/10.1029/2019RG000660>
- Bhandari, J., China, S., Girotto, G., Scarnato, B. V., Gorkowski, K., Aiken, A. C., Dubey, M. K., & Mazzoleni, C. (2019). Optical properties and radiative forcing of fractal-like tar ball aggregates from biomass burning. *Journal of Quantitative Spectroscopy and Radiative Transfer*, *230*, 65-74. <https://doi.org/https://doi.org/10.1016/j.jqsrt.2019.01.032>
- Cheng, Z., Morgenstern, M., Zhang, B., Fraund, M., Lata, N. N., Brimberry, R., Marcus, M. A., Mazzoleni, L., Fialho, P., Henning, S., Wehner, B., Mazzoleni, C., & China, S. (2022). Particles' phase state variability in the North Atlantic free troposphere during summertime determined by different atmospheric transport patterns and sources. *Atmos. Chem. Phys. Discuss.*, *2022*, 1-38. <https://doi.org/10.5194/acp-2022-84>
- China, S., Scarnato, B., Owen, R. C., Zhang, B., Ampadu, M. T., Kumar, S., Dzepina, K., Dziobak, M. P., Fialho, P., Perlinger, J. A., Hueber, J., Helmig, D., Mazzoleni, L. R., & Mazzoleni, C. (2015). Morphology and mixing state of aged soot particles at a remote marine free troposphere site: Implications for optical properties. *Geophysical Research Letters*, *42*(4), 1243-1250. <https://doi.org/https://doi.org/10.1002/2014GL062404>
- Chylek, P., & Wong, J. (1995). Effect of absorbing aerosols on global radiation budget [<https://doi.org/10.1029/95GL00800>]. *Geophysical Research Letters*, *22*(8), 929-931. <https://doi.org/https://doi.org/10.1029/95GL00800>
- Di Biagio, C., Formenti, P., Doppler, L., Gaimoz, C., Grand, N., Ancellet, G., Attié, J. L., Bucci, S., Dubuisson, P., Fierli, F., Mallet, M., & Ravetta, F. (2016). Continental pollution in the Western Mediterranean basin: large variability of the aerosol single scattering albedo and influence on the direct shortwave radiative effect. *Atmos. Chem. Phys.*, *16*(16), 10591-10607. <https://doi.org/10.5194/acp-16-10591-2016>

- Dunlea, E. J., DeCarlo, P. F., Aiken, A. C., Kimmel, J. R., Peltier, R. E., Weber, R. J., Tomlinson, J., Collins, D. R., Shinozuka, Y., McNaughton, C. S., Howell, S. G., Clarke, A. D., Emmons, L. K., Apel, E. C., Pfister, G. G., van Donkelaar, A., Martin, R. V., Millet, D. B., Heald, C. L., & Jimenez, J. L. (2009). Evolution of Asian aerosols during transpacific transport in INTEX-B. *Atmos. Chem. Phys.*, 9(19), 7257-7287. <https://doi.org/10.5194/acp-9-7257-2009>
- Fialho, P., Freitas, M. C., Barata, F., Vieira, B., Hansen, A. D. A., & Honrath, R. E. (2006). The Aethalometer calibration and determination of iron concentration in dust aerosols. *Journal of Aerosol Science*, 37(11), 1497-1506. <https://doi.org/https://doi.org/10.1016/j.jaerosci.2006.03.002>
- Fialho, P., Hansen, A. D. A., & Honrath, R. E. (2005). Absorption coefficients by aerosols in remote areas: a new approach to decouple dust and black carbon absorption coefficients using seven-wavelength Aethalometer data. *Journal of Aerosol Science*, 36(2), 267-282. <https://doi.org/https://doi.org/10.1016/j.jaerosci.2004.09.004>
- Hansen, A. D. A. (2005). *The Aethalometer, Manual*. Magee Scientific. [https://www.psi.ch/sites/default/files/import/lac/ProjectAddOnCatcosOperationsEN/Aethalometer\\_book\\_2005.07.02.pdf](https://www.psi.ch/sites/default/files/import/lac/ProjectAddOnCatcosOperationsEN/Aethalometer_book_2005.07.02.pdf)
- Honrath, R. E., Owen, R. C., Val Martín, M., Reid, J. S., Lapina, K., Fialho, P., Dziobak, M. P., Kleissl, J., & Westphal, D. L. (2004). Regional and hemispheric impacts of anthropogenic and biomass burning emissions on summertime CO and O<sub>3</sub> in the North Atlantic lower free troposphere [<https://doi.org/10.1029/2004JD005147>]. *Journal of Geophysical Research: Atmospheres*, 109(D24). <https://doi.org/https://doi.org/10.1029/2004JD005147>
- Kaskaoutis, D. G., Kambezidis, H. D., Hatzianastassiou, N., Kosmopoulos, P. G., & Badarinath, K. V. S. (2007). Aerosol climatology: dependence of the Angstrom exponent on wavelength over four AERONET sites. *Atmos. Chem. Phys. Discuss.*, 2007, 7347-7397. <https://doi.org/10.5194/acpd-7-7347-2007>
- Lenoble, J., Tanre, D., Deschamps, P. Y., & Herman, M. (1982). A Simple Method to Compute the Change in Earth-Atmosphere Radiative Balance Due to a Stratospheric Aerosol Layer. *Journal of Atmospheric Sciences*, 39(11), 2565-2576. [https://doi.org/10.1175/1520-0469\(1982\)039<2565:ASMTCT>2.0.CO;2](https://doi.org/10.1175/1520-0469(1982)039<2565:ASMTCT>2.0.CO;2)
- Liu, C., Chung, C. E., Yin, Y., & Schnaiter, M. (2018). The absorption Ångström exponent of black carbon: from numerical aspects. *Atmos. Chem. Phys.*, 18(9), 6259-6273. <https://doi.org/10.5194/acp-18-6259-2018>
- Mahowald, N., Albani, S., Kok, J. F., Engelstaeder, S., Scanza, R., Ward, D. S., & Flanner, M. G. (2014). The size distribution of desert dust aerosols and its impact on the Earth system. *Aeolian Research*, 15, 53-71. <https://doi.org/https://doi.org/10.1016/j.aeolia.2013.09.002>
- Masson-Delmotte, V., Zhai, P., Pirani, A., Connors, S. L., Péan, C., Berger, S., Caud, N., Chen, Y., Goldfarb, L., Gomis, M. I., Huang, M., Leitzell, K., Lonnoy, E., Matthews, J. B. R., Maycock, T. K., Waterfield, T., Yelekçi, O., Yu, R., Zhou, B., & (eds.). (2021). *IPCC, 2021: Climate Change 2021: The Physical Science Basis. Contribution of Working Group I to the Sixth Assessment Report of the Intergovernmental Panel on Climate Change*. C. U. Press.

- Mitchell, J. M. (1971). The Effect of Atmospheric Aerosols on Climate with Special Reference to Temperature near the Earth's Surface. *Journal of Applied Meteorology and Climatology*, 10(4), 703-714. [https://doi.org/10.1175/1520-0450\(1971\)010<0703:TEOAAO>2.0.CO;2](https://doi.org/10.1175/1520-0450(1971)010<0703:TEOAAO>2.0.CO;2)
- Moosmüller, H., & Ogren, J. A. (2017). Parameterization of the Aerosol Upscatter Fraction as Function of the Backscatter Fraction and Their Relationships to the Asymmetry Parameter for Radiative Transfer Calculations. *Atmosphere*, 8(8). <https://doi.org/10.3390/atmos8080133>
- Myhre, G., Samset, B. H., Schulz, M., Balkanski, Y., Bauer, S., Bernsten, T. K., Bian, H., Bellouin, N., Chin, M., Diehl, T., Easter, R. C., Feichter, J., Ghan, S. J., Hauglustaine, D., Iversen, T., Kinne, S., Kirkevåg, A., Lamarque, J. F., Lin, G., . . . Zhou, C. (2013). Radiative forcing of the direct aerosol effect from AeroCom Phase II simulations. *Atmos. Chem. Phys.*, 13(4), 1853-1877. <https://doi.org/10.5194/acp-13-1853-2013>
- Nemesure, S., Wagener, R., & Schwartz, S. E. (1995). Direct shortwave forcing of climate by the anthropogenic sulfate aerosol: Sensitivity to particle size, composition, and relative humidity [<https://doi.org/10.1029/95JD02897>]. *Journal of Geophysical Research: Atmospheres*, 100(D12), 26105-26116. <https://doi.org/https://doi.org/10.1029/95JD02897>
- Pavese, G., f.esposito, Calvello, M., & Gueguen, E. (2012). A new algorithm for brown and black carbon identification and organic carbon detection in fine atmospheric aerosols by a multi-wavelength Aethalometer. *Atmospheric Measurement Techniques Discussion*, 5, 1003-1027. <https://doi.org/10.5194/amtd-5-1003-2012>
- Redmond, H. E., Dial, K. D., & Thompson, J. E. (2010). Light scattering and absorption by wind blown dust: Theory, measurement, and recent data. *Aeolian Research*, 2(1), 5-26. <https://doi.org/https://doi.org/10.1016/j.aeolia.2009.09.002>
- Riemer, N., & West, M. (2013). Quantifying aerosol mixing state with entropy and diversity measures. *Atmos. Chem. Phys.*, 13(22), 11423-11439. <https://doi.org/10.5194/acp-13-11423-2013>
- Rudich, Y., Donahue, N. M., & Mentel, T. F. (2007). Aging of Organic Aerosol: Bridging the Gap Between Laboratory and Field Studies. *Annual Review of Physical Chemistry*, 58(1), 321-352. <https://doi.org/10.1146/annurev.physchem.58.032806.104432>
- Sagan, C. E., & Pollack, J. B. (1967). Anisotropic nonconservative scattering and the clouds of Venus. *Journal of Geophysical Research*, 72, 469-477.
- Schum, S. K., Zhang, B., Džepina, K., Fialho, P., Mazzoleni, C., & Mazzoleni, L. R. (2018). Molecular and physical characteristics of aerosol at a remote free troposphere site: implications for atmospheric aging. *Atmos. Chem. Phys.*, 18(19), 14017-14036. <https://doi.org/10.5194/acp-18-14017-2018>
- Seinfeld, J. H., & Pandis, S. N. (2016). *Atmospheric Chemistry and Physics: From Air Pollution to Climate Change*. Wiley. [https://books.google.com/books?id=n\\_RmCgAAQBAJ](https://books.google.com/books?id=n_RmCgAAQBAJ)
- Stohl, A., Forster, C., Frank, A., Seibert, P., & Wotawa, G. (2005). Technical note: The Lagrangian particle dispersion model FLEXPART version 6.2. *Atmos. Chem. Phys.*, 5(9), 2461-2474. <https://doi.org/10.5194/acp-5-2461-2005>

- Uin, J. (2016). *Integrating Nephelometer Instrument Handbook*. United States Retrieved from <https://www.osti.gov/biblio/1246075>
- Wiscombe, W. J., & Grams, G. W. (1976). The Backscattered Fraction in two-stream Approximations. *Journal of Atmospheric Sciences*, 33(12), 2440-2451. [https://doi.org/10.1175/1520-0469\(1976\)033<2440:TBFITS>2.0.CO;2](https://doi.org/10.1175/1520-0469(1976)033<2440:TBFITS>2.0.CO;2)
- Yao, Y., Curtis, J., Ching, J., Zheng, Z., & Riemer, N. (2022). Quantifying the effects of mixing state on aerosol optical properties. *Atmos. Chem. Phys. Discuss.*, 2022, 1-24. <https://doi.org/10.5194/acp-2022-131>
- Yu, X., Shen, L., Xiao, S., Ma, J., Lü, R., Zhu, B., Hu, J., Chen, K., & Zhu, J. (2019). Chemical and Optical Properties of Atmospheric Aerosols during the Polluted Periods in a Megacity in the Yangtze River Delta, China. *Aerosol and Air Quality Research*, 19(1), 103-117. <https://doi.org/10.4209/aaqr.2017.12.0572>
- Zhang, B., Owen, R. C., Perlinger, J. A., Helmig, D., Val Martín, M., Kramer, L., Mazzoleni, L. R., & Mazzoleni, C. (2017). Ten-year chemical signatures associated with long-range transport observed in the free troposphere over the central North Atlantic. *Elementa: Science of the Anthropocene*, 5. <https://doi.org/10.1525/elementa.194>
- Zhang, B., Owen, R. C., Perlinger, J. A., Kumar, A., Wu, S., Val Martin, M., Kramer, L., Helmig, D., & Honrath, R. E. (2014). A semi-Lagrangian view of ozone production tendency in North American outflow in the summers of 2009 and 2010. *Atmos. Chem. Phys.*, 14(5), 2267-2287. <https://doi.org/10.5194/acp-14-2267-2014>
- Zheng, G., Sedlacek, A. J., Aiken, A. C., Feng, Y., Watson, T. B., Raveh-Rubin, S., Uin, J., Lewis, E. R., & Wang, J. (2020). Long-range transported North American wildfire aerosols observed in marine boundary layer of eastern North Atlantic. *Environment international*, 139, 105680. <https://doi.org/10.1016/j.envint.2020.105680>
- Zhou, S., Collier, S., Jaffe, D. A., & Zhang, Q. (2019). Free tropospheric aerosols at the Mt. Bachelor Observatory: more oxidized and higher sulfate content compared to boundary layer aerosols. *Atmos. Chem. Phys.*, 19(3), 1571-1585. <https://doi.org/10.5194/acp-19-1571-2019>

## A Appendix

### A.1 Elemental Classification of Samples

Aerosol particles were classified into eight different types depending on their chemical composition. The different types were based on the following criteria (all values are weight percent composition):

1. OC (carbon and oxygen):  $Na < 0.5$  and  $\sum (C, N, O) > 97$  and  $N < 5$
2. CNO (carbon, nitrogen, and oxygen):  $Na < 0.5$  and  $\sum (C, N, O) > 97$  and  $N \geq 5$
3. CNOS (carbon, nitrogen, and sulfur):  $Na < 0.5$  and  $\sum (Mg, Al, Si, P, Cl, K, Ca, Mn, Fe, Zn) < 1$  and  $S \geq 0.5$
4. Sea Salt:  $Na \geq 0.5$  and  $Na \geq S$  and  $Na > \sum (Al, Si, Ca, Fe, Mn, Zn)$
5. Sea Salt/Sulfur:  $Na \geq 0.5$  and  $Na < S$  and  $Na > \sum (Al, Si, Ca, Fe, Mn, Zn)$
6. Dust:  $Na \leq \sum (Al, Si, Ca, Fe)$  and  $\sum (Al, Si, Ca, Fe) \geq 4$
7. Dust with Sulfur:  $Na \leq \sum (Al, Si, Ca, Fe)$  and  $\sum (Mg, Al, Si, P, Cl, K, Ca, Mn, Fe, Zn) < 15$  and  $S > 1$  and  $\sum (Al, Si, Ca, Fe) \geq 2$
8. Other: does not fit in prior categories

### A.2 Correction of C, N, and O

The EDX measurement of C, N, and O is semi-quantitative and there is contribution of C and O from the B-film, so post-correction factors need to be performed. This correction was estimated by using CNQX disodium salt as a standard material, which contains not only C, N, and O, but also Na that can be analyzed quantitatively. Post-correction functions for C, N, and O were found to be:

$$C_{\text{real}} = (123.2 \pm 1.4) - (4.738 \pm 0.214) \log(H) - (1.186 \pm 0.02)C_{\text{measured}} \quad \text{Eq. 21}$$

$$O_{\text{real}} = (13.68 \pm 0.18) - (0.3413 \pm 0.0636) \log(H) + (0.2579 \pm 0.0072)O_{\text{measured}} \quad \text{Eq. 22}$$

$$N_{\text{real}} = (1.101 \pm 0.002)N_{\text{measured}} \quad \text{Eq. 23}$$

Where  $C_{\text{measured}}$ ,  $N_{\text{measured}}$ , and  $O_{\text{measured}}$  are the measured atomic percentages of C, N, and O;  $C_{\text{real}}$ ,  $N_{\text{real}}$ , and  $O_{\text{real}}$  are the expected atomic percentages of C, N, and O; and  $H$  is the height of the particle ( $\mu\text{m}$ ). The area equivalent diameter is approximately equal to the height,  $H$ . The height is therefore determined by normalizing the longest measured area equivalent diameter by the aspect ratio of the sample, which is determined using a tilted ( $70^\circ$ ) image of the sample. These are calculated based on the stoichiometric ratio between each respective element and Na.

### A.3 Nephelometer LED Spectral Power Distribution Curves

Figure 9 shows the LED (LUXEON Rebel) spectral power distribution for the three nephelometer wavelengths. The colors are red, green, and royal blue, corresponding to 635 nm, 525 nm, and 450 nm center wavelengths respectively. These distributions were used to calculate the weighted averages of the spectral solar irradiances reported in A.4.



Figure 9: The relative spectral power distribution curves for the Aurora 3000 nephelometer LEDs.

#### A.4 Aerosol Forcing Parameter Values

The calculation of the aerosol spectral radiative forcing (Eq. 3) used values for  $T_{\text{atm}}$ ,  $A_{\text{cld}}$ , and  $R_{\text{surf}}$  from (China et al., 2015). The AOD ( $\tau$ ) was estimated from the Aerosol Robotic Network (AERONET) data from the Atmospheric Radiation Measurement (ARM) site<sup>2</sup> at Graciosa, another island in the Azores. The solar irradiance values were determined using the 2000 ASTM Standard Extraterrestrial Spectrum Reference E-490-00<sup>3</sup> and the relative spectral power distributions of the Aurora 3000 nephelometer LEDs (A.3). The values used were:

$$\langle \Delta S / \Delta \lambda \rangle_{450} = 1.953 * 10^{-3} \text{ W m}^{-2} \text{ nm}^{-1}$$

$$\langle \Delta S / \Delta \lambda \rangle_{525} = 1.853 * 10^{-3} \text{ W m}^{-2} \text{ nm}^{-1}$$

$$\langle \Delta S / \Delta \lambda \rangle_{635} = 1.623 * 10^{-3} \text{ W m}^{-2} \text{ nm}^{-1}$$

$$T_{\text{atm}} = 0.79$$

$$A_{\text{cld}} = 0.6$$

$$R_{\text{surf}} = 0.06 \text{ (ocean)}$$

$$R_{\text{surf}} = 0.8 \text{ (cloud)}$$

$$\tau = 0.1$$

<sup>2</sup> [AERONET Aerosol Optical Depth Data Display Interface \(nasa.gov\)](https://aeronet.gsfc.nasa.gov/)

<sup>3</sup> [2000 ASTM Standard Extraterrestrial Spectrum Reference E-490-00 | Grid Modernization | NREL](https://www.astm.org/standards/E490-00.html)